Journal of Zhejiang University-SCIENCE A (Applied Physics & Engineering)
ISSN 1673-565X (Print); ISSN 1862-1775 (Online)
www.zju.edu.cn/jzus; www.springerlink.com
E-mail: jzus@zju.edu.cn

# Experimental study of the pinned double rectangular tube assembled buckling-restrained brace*

Zi-qin JIANG†1, Yan-lin GUO[2], Ai-lin ZHANG[1,3], Chao DOU[4], Cai-xia ZHANG[5]

([1]*College of Architecture and Civil Engineering, Beijing University of Technology, Beijing 100124, China*)

([2]*Department of Civil Engineering, Tsinghua University, Beijing 100084, China*)

([3]*Beijing Engineering Research Center of High-rise and Large-span Prestressed Steel Structure, Beijing University of Technology, Beijing 100124, China*)

([4]*School of Civil Engineering, Beijing Jiaotong University, Beijing 100044, China*)

([5]*Beijing Key Laboratory of Advanced Manufacturing Technology, Beijing University of Technology, Beijing 100124, China*)

†E-mail: jzqbj2010@163.com

Received June 30, 2016; Revision accepted Nov. 9, 2016; Crosschecked Dec. 13, 2016

**Abstract:** In this study, seven pinned double-rectangular tube assembled buckling-restrained brace (DRT-ABRB) specimens were experimentally characterised by means of an axial cyclic test. The core member of the specimens was a single flat-plate. Two rectangular tubes were assembled using high strength bolts to form an external restraining member. Each rectangular tube was composed of an external steel channel and a cover plate. A gap or thin rubber filler was set between the core and the external restraining member to form an unbonded layer. The influence of several design parameters on the failure mode and energy dissipation capacity of the ABRB was investigated, including the height of the core wing plate, thickness of the external cover plate, and height of the external channel flange. This experimental study demonstrated that a local pressure-bearing failure at the end of the external member arises when the external cover plate is too thin or if the end construction detail is unreasonable. When the end rotations of the DRT-ABRB were restricted, the hysteretic performance was shown to be superior to that of a pure pinned DRT-ABRB. Finally, all the tested DRT-ABRBs exhibited excellent energy dissipation performance which amply satisfied existing regulation requirements.

**Key words:** Double-rectangular tube assembled buckling-restrained brace (DRT-ABRB); Construction detail; Hysteretic behaviour; Failure mode; High strength bolt

http://dx.doi.org/10.1631/jzus.A1600483 **CLC number:** TU391

## 1 Introduction

Buckling-restrained braces (BRBs) provide a means to overcome the inherent instability of ordinary braces subject to pressure loads and enhance the energy dissipation capacity of a frame brace structure. As a result, BRBs have been widely used in the engineering field (Black *et al.*, 2004; Xie, 2005; Tremblay *et al.*, 2006; Di Sarno and Manfredi, 2010; 2012). A BRB can provide a frame structure with stable lateral resistance stiffness and bearing capacity. Its hysteresis curve also shows symmetry properties, which can effectively avoid the unbalanced force of the frame beam caused by brace instabilities.

The buckling-restrained concept was first proposed in an experimental study of a steel plate brace precast in a shear wall (Yoshino and Kano, 1971). Subsequently, Kimura *et al.* (1976) applied this concept to a brace and conducted an experimental investigation on a BRB with a single flat-plate core

* Project supported by the National Natural Science Foundation of China (Nos. 51178243 and 51608014), the China Postdoctoral Science Foundation (No. 2015M580030), and the Natural Science Foundation of Beijing, China (No. 8131002)

ORCID: Zi-qin JIANG, http://orcid.org/0000-0001-9613-3972

member and a rectangular steel pipe filled with mortar as the external restraining member. Further experiments were conducted on various forms of BRBs to obtain a more comprehensive understanding of the influence of different cross-section forms, design parameters, and configuration forms on the energy dissipation performance of a BRB (Chen *et al.*, 2001; Inoue *et al.*, 2001; Black *et al.*, 2004; Iwata and Murai, 2006; Fahnestock *et al.*, 2007; Tsai and Hsiao, 2008; Di Sarno and Elnashai, 2009; Ju *et al.*, 2009; Chou and Chen, 2010; Sun *et al.*, 2011; Zhao *et al.*, 2011; 2012; Wang *et al.*, 2012). BRBs can be classified into two categories based on the composition of the external restraining member: integrated BRBs (Chen *et al.*, 2001; Black *et al.*, 2004; Iwata and Murai, 2006; Tremblay *et al.*, 2006; Ju *et al.*, 2009; Sun *et al.*, 2011; Jiang *et al.*, 2015a; 2015b) and assembled BRBs (Eryaşar, and Topkaya, 2009; Chou and Chen, 2010; Hoveidae and Rafezy, 2012; Usami *et al.*, 2012; Wang *et al.*, 2013; Jiang *et al.*, 2017).

Assembled BRBs have gradually become a popular subject of research as they can effectively avoid a series of issues affecting traditional BRBs, such as the need for higher precision control between the external concrete member and the core steel member, and the heavy workload of wet concrete operations. As the external restraining member of an assembled BRB is primarily connected via high strength bolts, the assembly may be conducted on-site. This greatly enhances the flexibility of member transportation and installation, and facilitates core member replacement after an earthquake. Usami *et al.* (2012) and Wang *et al.* (2013) conducted cyclic loading tests to study the detailed construction rationality of a double cover plate assembled BRB. Chou and Chen (2010) performed a cyclic loading test on a double rectangular tube assembled BRB with in-fill concrete and investigated the influence of the bolt spacing arrangement and external restraining rigidity on its performance. Eryaşar and Topkaya (2009) also conducted some experiments on an assembled BRB with multiple cross-section forms.

Guo and Wang (2010) proposed a double-rectangular tube assembled buckling-restrained brace (DRT-ABRB). Seven pinned DRT-ABRBs were studied using axial cycle tests to understand the influence of the external cover plate thickness, core wing plate height, external channel flange height and other design parameters on the failure mechanisms and energy dissipation performance of the BRBs. The rationality of the end construction detail was verified, and the DRT-ABRB energy dissipation performance was determined. These results laid a foundation for engineering applications of DRT-ABRBs.

## 2 Layouts of the DRT-ABRB

Each DRT-ABRB is composed of an internal core member (which is subjected to an axial pressure), external restraining members (which can prevent the internal core from buckling), and an unbonded material between them (Fig. 1). The external restraining members of the DRT-ABRB consist of an upper and a lower rectangular tube, each of which is fastened via high-strength bolts and cushion blocks. The external rectangular tube can be soldered by using a cover plate and channel steel or four flat plates. The external cover plate should be wider than the internal core member to enable the bolts to be fastened easily. The corresponding holes should be set in the extension place, in which the bolts are arranged along the longitudinal direction of the member, and a pair of strengthening bolts should be added to the external end to ensure a reliable connection between the upper and lower rectangular tubes.

The core member is a single flat plate. The extension part at the end of the core member is strengthened by means of two wing plates. To ensure that the strengthened section of the core member can stretch out and draw back flexibly in the vertical direction, the end of the upper and lower cover plates of the rectangular tube should be slotted. In addition, the slotted part should be strengthened by a channel head plate and a channel stiffener, and its length should be equal to that of the strengthened part. A gap must be present between the internal core member and the external restraining members. The size of the gap can be adjusted by changing the thickness of the cushion blocks to form an unbonded layer. To inhibit the external restraining member from sliding along in the direction of the core member, a stopper must be set on both sides. A hole in the corresponding position of each stopper should also be set in the middle of the external cover plate.

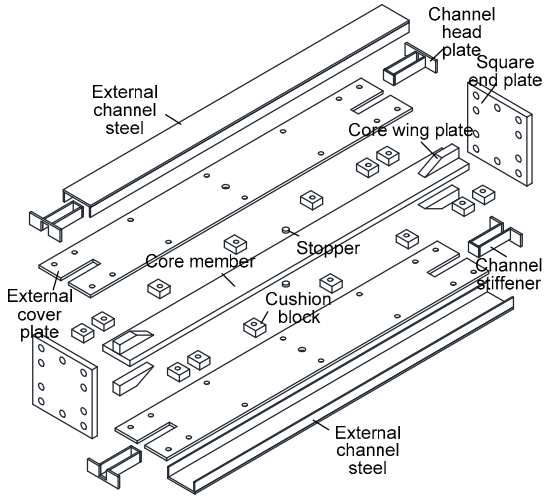


**Fig. 1 3D exploded view of the DRT-ABRB**

Fig. 2 shows a schematic diagram of the assembled BRB and the basic size parameters. The core member weak axis ($x$ axis) corresponds to the main bending direction of the external member; $h_{cp}$ denotes the width and $t_{cp}$ the thickness of the cover plate; $h_{ud}$ denotes the web height and $t_{udh}$ the thickness of the channel steel; $b_{ud}$ denotes the flange width and $t_{udb}$ its equivalent thickness; $h_c$ denotes the width and $t_c$ the thickness of the core member; $b_0$ denotes the width and $t_0$ the thickness of the wing plate.

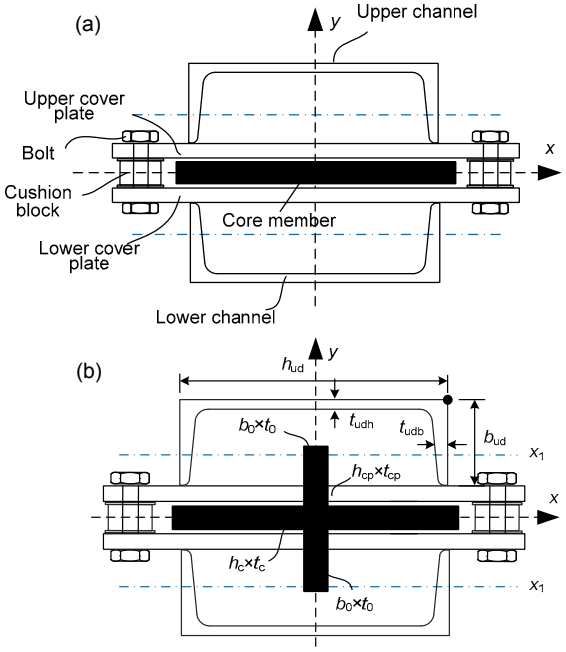


**Fig. 2 Schematic diagram of the DRT-ABRB**
(a) Mid-span section; (b) End section

## 3 Test program

### 3.1 Specimen design

The specimens were connected by a pinned joint and a loading device. For the joint design, it was necessary to consider the following aspects: joint design tonnage, end plate bolt number, ear plate size, and pin diameter. After analyzing the design, a 50-mm-thick Q345B end plate with a size of 400 mm ×400 mm was selected. Ten 10.9 M30 high strength bolts were used to connect the pinned joint to the specimens. The pin had a diameter of 80 mm and was made of No. 45 steel. The relevant dimensions of the pinned joint are shown in Fig. 3.

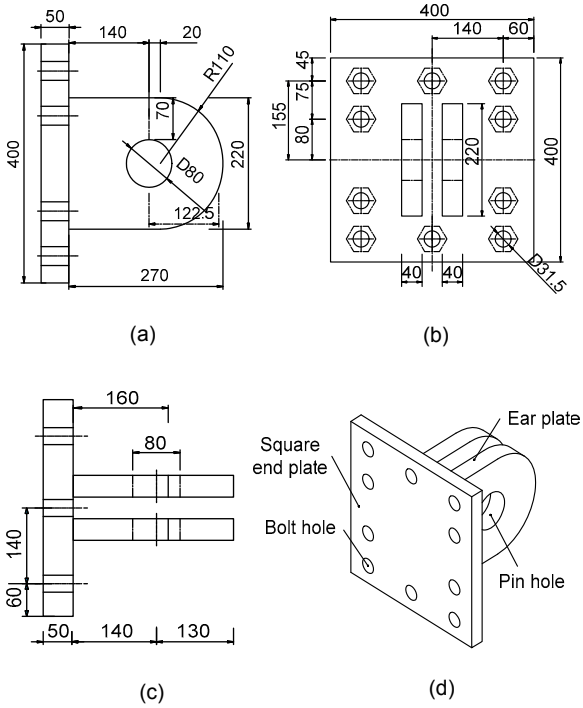


**Fig. 3 Diagram of the ABRB pinned joint (unit: mm)**
(a) Front view; (b) Side view; (c) Top view; (d) 3D diagram

In this section, the energy dissipation performance of seven BRB specimens is investigated. Details of the specimens' construction are shown in Fig. 4. The relevant parameters of the specimens are listed in Table 1 and the meaning of each parameter is shown in Fig. 2. $L_{em}$ represents the length of the external restraining member, $\zeta_{x,\mu}$ is the restraining ratio of the BRB (Jiang *et al.*, 2015c), and the influence of the external restraining rigidity reduction coefficient is considered as

$$\xi_{x,\mu}=\frac{\mu\pi^2 E_{\mathrm{b}} I_{\mathrm{b}}}{L_{\mathrm{BRB}}^2 N_{\mathrm{y}}}, \tag{1}$$

where $\mu$ is the external restraining rigidity reduction coefficient of the DRT-ABRB (Guo *et al.*, 2015), and the influence of the discrete arrangement of the bolts is considered. $E_{\mathrm{b}}I_{\mathrm{b}}$ is the flexural rigidity of the external restraining member when the influence of the bolt arrangement is ignored. $L_{\mathrm{BRB}}$ is the distance between two pinned joints of the ABRB, and $N_{\mathrm{y}}$ is the yield load of the core member.

Note that a 2 mm gap was set between the core member of the specimens (PABRB1–PABRB6) and the external restraining members on both sides. Moreover, specimens PABRB7-Ru and PABRB1 had the same cross-sectional parameters, except that the unbounded layer had thin rubber as filling material.

A construction drawing of the PABRB1 specimen is shown in Fig. 5, and an operation drawing of the BRB specimen in Fig. 6. The core member of the DRT-ABRB was a Q235 steel flat plate with a cross-section of 160 mm×30 mm, and length $L_{\mathrm{cm}}$ of 2 m. A 40-mm-thick Q235 steel wing plate with a 1:2 groove was welded at the end of the core member. The dimensions of the plate were 200 mm×50 mm (Fig. 5). The lengths of the uniform and variable sections of the strengthened core region were both 100 mm. A 2 mm gap was set between the core member and the external cover plates and between the core member and the cushion blocks. The core member and the core wing plate were welded to the square end plates on both sides (Fig. 6a). Two stoppers were welded on each side of the mid-span of the core member. The end plate was a 40-mm-thick Q345 steel plate with holes of 31.5 mm diameter.

The external restraining member of the specimens was composed of an external cover plate, external channel steel, channel head plate, and channel stiffener. Except for the external channel steel, which was made of Q235 steel, the other components were made of Q345 steel. Several bolt holes with a diameter of 21.5 mm were set on the external cover plate along the longitudinal direction of the DRT-ABRB. The core wing plates on each side of this plate were slotted and locally strengthened through the channel

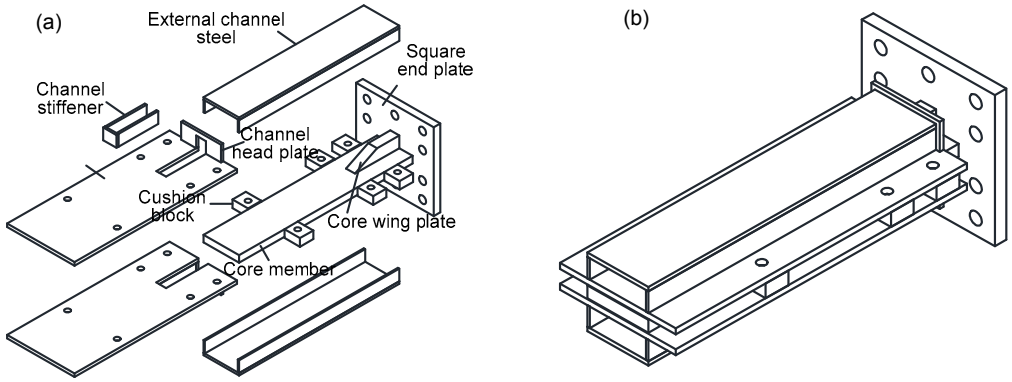


**Fig. 4 Construction details of specimens: (a) exploded view; (b) assembly drawing**

**Table 1 Parameters of specimens**

| Specimen | $h_{\mathrm{c}}$ (mm) | $t_{\mathrm{c}}$ (mm) | $h_{\mathrm{cp}}$ (mm) | $t_{\mathrm{cp}}$ (mm) | $h_{\mathrm{ud}}$ (mm) | $t_{\mathrm{udh}}$ (mm) | $b_{\mathrm{ud}}$ (mm) | $t_{\mathrm{udb}}$ (mm) | $b_0$ (mm) | $L_{\mathrm{em}}$ (mm) | Bolt | $\mu$ | $\xi_{x,\mu}$ |
|---|---|---|---|---|---|---|---|---|---|---|---|---|---|
| PABRB1 | 160 | 30 | 304 | 12 | 160 | 6.5 | 63 | 10 | 50 | 1920 | $7^{*1}$ | 0.431 | 3.43 |
| PABRB2 | 160 | 30 | 304 | 10 | 160 | 6.5 | 63 | 10 | 50 | 1920 | $7^{*1}$ | 0.430 | 3.16 |
| PABRB3 | 160 | 30 | 304 | 12 | 160 | 6.5 | 50 | 10 | 50 | 1920 | $7^{*1}$ | 0.399 | 2.31 |
| PABRB4 | 160 | 30 | 304 | 12 | 160 | 6.5 | 63 | 10 | 40 | 1920 | $7^{*1}$ | 0.431 | 3.43 |
| PABRB5 | 160 | 30 | 304 | 12 | 160 | 6.5 | 63 | 10 | 50 | 1900 | $7^{*1}$ | 0.430 | 3.42 |
| PABRB6 | 160 | 30 | 304 | 12 | 160 | 6.5 | 63 | 10 | 50 | 1920 | $7^{*0}$ | 0.482 | 3.84 |
| PABRB7-Ru | 160 | 30 | 304 | 12 | 160 | 6.5 | 63 | 10 | 50 | 1920 | $7^{*1}$ | 0.431 | 3.43 |

Note: The number in the bolt column represents the total number of bolts that are arranged along the longitudinal direction of DRT-ABRB, $^{*1}$ states that the local strengthened bolts are set on end sides, and $^{*0}$ indicates that the bolts are equidistantly arranged along the longitudinal direction

stiffener. Taking 10 mm as the stiffener thickness, the channel stiffener, external cover plate, and channel head plate were connected via fillet weld connections (Fig. 6b). Taking 10 mm as the thickness of the channel head plate, the channel head plate and the external cover plate were bound via groove welds. The external channel steel took [16a (the channel height is 160 mm, channel width is 63 mm, web thickness is 6.5 mm, and flange thickness is 10 mm), and the external channel steel, external cover plate, and the channel head plate were bound via fillet welds. The upper and lower external members were closely linked to the core member and were connected by grade 10.9 M20 high strength bolts. The cushion blocks, controlling the distance between the upper and lower external members (Fig. 6c), were also made of Q345 steel plate with holes of 21.5 mm diameter.

### 3.2 Material properties

According to the requirements of GB/T228.1-2010 (SAC, 2010), the material properties tests of the core and external members of variable thicknesses were conducted. The corresponding material property index is shown in Table 2, in which $f_y$ denotes the steel yield strength, $f_u$ the steel tensile strength, and $f_u/f_y$ the steel tensile-yield strength ratio.

### 3.3 Test scheme

The hysteresis experiment was conducted using a 600 t tension and compression actuator at the

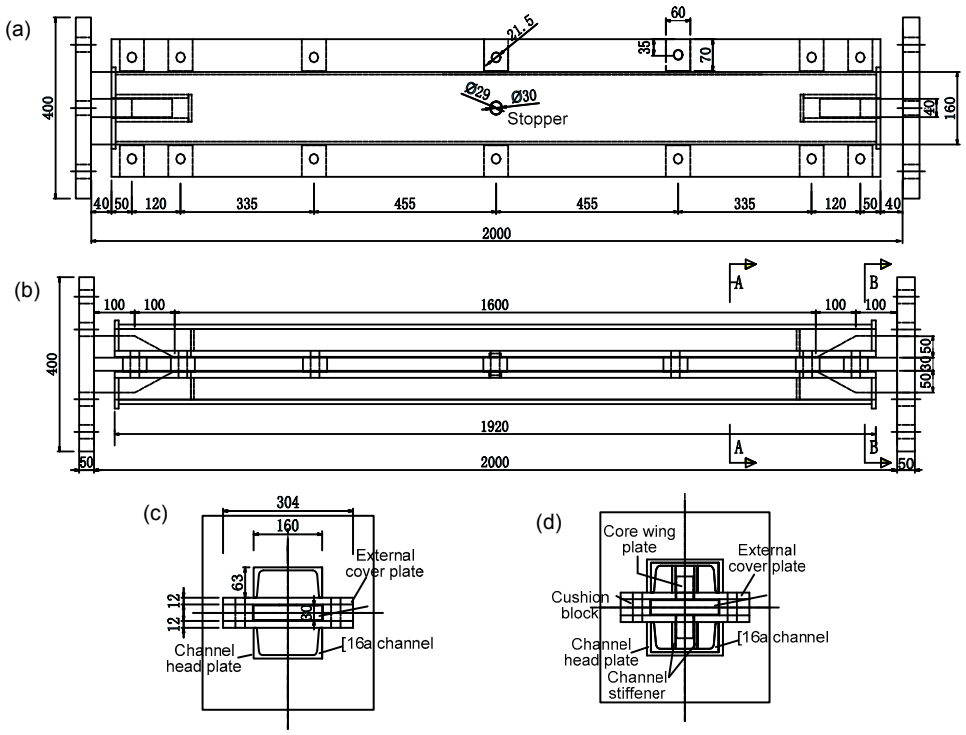


**Fig. 5 Construction drawing of the PABRB1**
(a) Top view; (b) Front view; (c) A-A section; (d) B-B section

(a) (b) (c)

**Fig. 6 Construction of the DRT-ABRB specimen**
(a) Core construction; (b) Slotted part construction; (c) End construction

Structure Laboratory of Tsinghua University, China. Both ends of the specimens were connected to the actuator and reaction frames through a flange and pinned joints (Fig. 7). The flange of the pinned joint was constructed with a 50-mm-thick Q345 steel plate, and a 10.9 M30 high strength bolt was used as the connecting bolt.

To observe the rotational changes, an angle displacement meter was set at the end of the specimens. Two axial displacement meters were also set at the front and back of the specimens to observe the axial deformation. Five vertical displacement meters were equidistantly placed along the longitudinal direction of the specimens to measure the vertical deflection.

The loading law adopted in this test may be divided into two stages (Fig. 8). The first stage corresponded to an amplitude increment loading stage, in which two loading cycles were performed to induce a progressive increase in the core axial strains of 0.25%, 0.50%, 0.75%, 1.00%, 1.50%, 2.00%, 2.50%, and 3.00%. In the second stage, three loading cycles were performed with a 2.00% core axial strain followed by a single cycle of 4.00% strain to complete the experiment. According to this loading law, when the DRT-ABRB specimens completed two 2.00% axial strain loadings, the value of their cumulative plastic deformation capability was measured at 372; when completing the two cycles at 3.00% axial strain, the cumulative plastic deformation reached 742. These measurements satisfy the plastic deformation capability requirements on the BRB specified in ANSI/AISC 341-10 (AISC, 2010). The core length of the specimens was 2.0 m, and the core yield region length was 1.6 m. The core axial displacement loading law of each specimen is shown in Table 3.

**Table 2 Mechanical properties of the steel plate**

| Plate position | Thickness (mm) | Steel type | $f_y$ (MPa) | $f_u$ (MPa) | $f_u/f_y$ |
|---|---|---|---|---|---|
| Channel web | 6 | Q235 | 264 | 408 | 1.55 |
| External cover plate | 10 | Q345 | 395 | 542 | 1.37 |
| External cover plate | 12 | Q345 | 368 | 502 | 1.36 |
| Core member | 30 | Q235 | 245 | 421 | 1.72 |
| Core wing plate | 40 | Q235 | 228 | 402 | 1.76 |

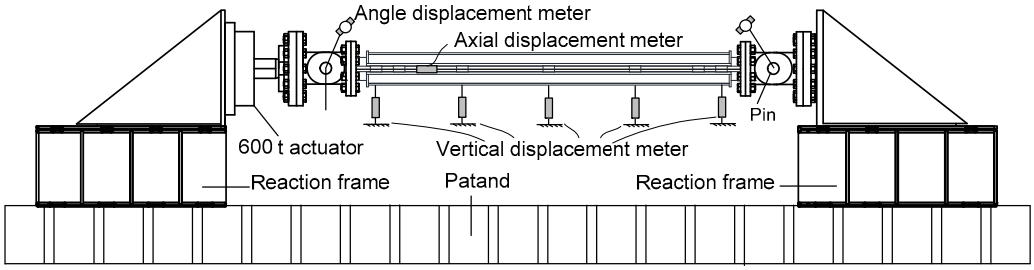


**Fig. 7 Loading scheme and sensors position**

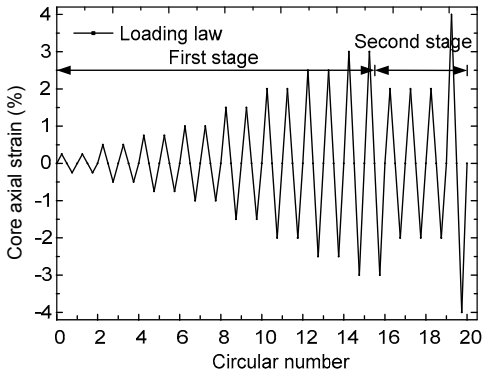


**Fig. 8 Test loading law**

**Table 3 Core axial displacement loading law**

| Hierarchical-loading | Cycle number | Axial strain | Axial displacement (mm) |
|---|---|---|---|
| 1 | 2 | ±0.25% | ±4.0 |
| 2 | 2 | ±0.50% | ±8.0 |
| 3 | 2 | ±0.75% | ±12.0 |
| 4 | 2 | ±1.00% | ±16.0 |
| 5 | 2 | ±1.50% | ±24.0 |
| 6 | 2 | ±2.00% | ±32.0 |
| 7 | 2 | ±2.50% | ±40.0 |
| 8 | 2 | ±3.00% | ±48.0 |
| 9 | 3 | ±2.00% | ±32.0 |
| 10 | 1 | ±4.00% | ±64.0 |

## 4 Test results and analysis

### 4.1 Failure mode and failure mechanism

The DRT-ABRB specimens in this study showed four failure modes: (1) extended strengthened core bending failure, (2) external end local pressure-bearing failure, (3) multi-wave local buckling failure, and (4) overall buckling failure (Fig. 9).

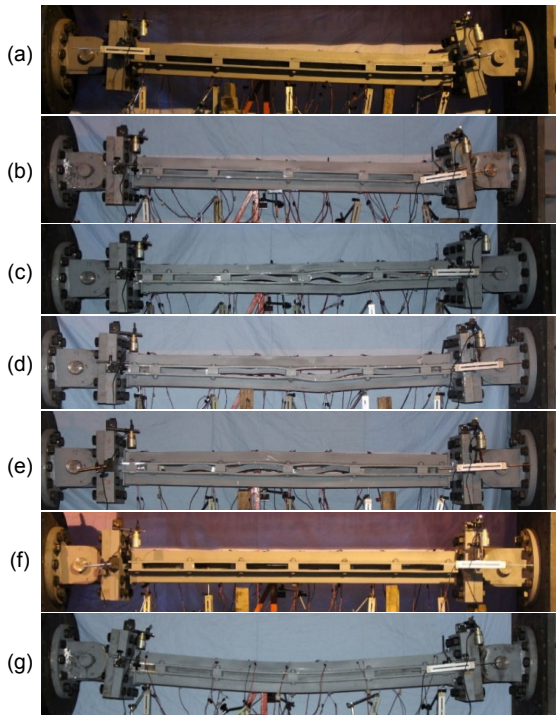


**Fig. 9 Specimens at the end of the loading cycle**
(a) PABRB1; (b) PABRB2; (c) PABRB3; (d) PABRB4; (e) PABRB5; (f) PABRB6; (g) PABRB7-Ru

PABRB1, PABRB2, and PABRB7-Ru exhibited the same failure modes: external end local pressure-bearing failure and overall buckling failure. A difference between specimens PABRB1 and PABRB7-Ru was related to the use of the rubber isolation layer. Except from the sound generated under the cyclic loading, these specimens showed a similar mechanical performance and underwent failure when being loaded to the second ring of 2.5% axial compressive strain (corresponding axial displacement of 40 mm).

Specimen PABRB1 had a relatively stable end rotation during the early loading stage. However, in the late loading stage, the right end rotation of the specimen showed a nonlinear growth trend and its extended core region underwent a bending failure. When the PABRB7-Ru specimen was loaded to the first ring of 40 mm, significant vertical distortions were observed. However, the specimen still had a stable bearing capacity and it underwent overall buckling failure at the beginning of the second loading cycle, when both ends showed significant angular distortions. The difference between the failure modes of these two specimens may have been caused by a difference in core frictional force and machining errors. The PABRB2 specimen underwent the expected local pressure-bearing failure, which occurred during the first loading cycle at 2.00% core axial strain and was caused mainly by the smaller thickness of the external cover plates. The external cover plate and channel head plate of this specimen were highly stretched and major local distortions were observed.

When the pinned joint is jammed, the end rotation of the specimens is limited and the core member exhibits an obvious multi-wave buckling deformation. This was the case for the PABRB3–6 specimens, which had a higher stability and bearing capacity than the other specimens tested. Except for the PABRB4 specimen, the specimens endured the complete loading law of the first stage. Fig. 9 shows that the external limb segments between the bolts of specimens PABRB3–PABRB5 were stretched and showed the multi-wave local buckling failure described above. In contrast, specimen PABRB4 underwent an earlier failure, mainly due to the lower stiffness of the strengthened core region, but the end rotation of the pinned joint was still visible. The uniform layout of the bolts enabled specimen PABRB6 to withstand the entire loading cycle with a core member deformation primarily composed of the multi-wave pattern. Note that the external member end of the pinned BRB will have a larger contact force, and more bolts need to be set at the external end. However, if the end rotation of the BRB is restricted, then the end contact force will decrease. Thus, the end of specimen PABRB6 did not suffer any damage.

The residual deformation of the core member could be observed only after disassembling the bolts (Fig. 10). Except for the core member of specimen PABRB7-Ru with the rubber filler, which had a single-wave deformation, each core member around

the weak axis showed multi-wave buckling deformation. In addition, the core members of all BRBs displayed almost no multi-wave deformations around their strong axis. This observation may be explained by the ratio between the multi-wave length and the core member width-to-thickness ratio. The core member around its strong axis wave will have a larger minimum half-wave length, thereby inhibiting multi-wave buckling deformation.

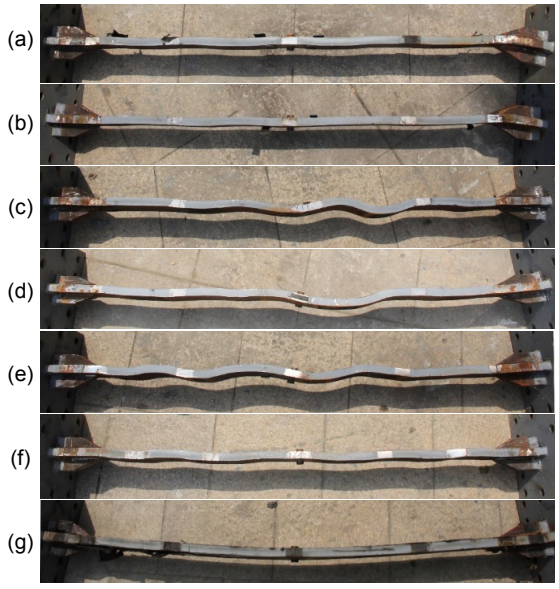


**Fig. 10 Residual deformation of the core member**
(a) PABRB1; (b) PABRB2; (c) PABRB3; (d) PABRB4; (e) PABRB5; (f) PABRB6; (g) PABRB7-Ru

### 4.2 Hysteresis curve

The hysteresis curves of the specimens are shown in Fig. 11. The vertical coordinate is the applied axial load of the BRB, with the sign convention of tension being positive and compression being negative. The horizontal coordinate is the measured axial deformation, with the same sign convention.

These hysteresis curves show that all the tested specimens had a relatively stable hysteretic behaviour, with a plump hysteresis curve and adequate energy dissipation capacity. Except for specimen PABRB2, no specimens showed a stiffness or strength degradation phenomenon when loaded at 2.0% of core axial strain. They showed nearly the same loading and unloading stiffness. In addition, the specimens showed a noticeable cyclic hardening characteristic, which became more visible during the compression phases. Further, the asymmetry between tension and compression was more noticeable for specimens PABRB3–PABRB6, in which the end rotation was restricted.

Comparison of the hysteresis curves of the specimens shows that the hysteresis energy dissipation performance of the pure pinned DRT-ABRB was poorer than that of the DRT-ABRB with restricted end rotation. However, the BRB with a rigid connection had a bending moment effect on the loading device which should be considered in the frame structure.

### 4.3 Mechanical properties of BRB

Through analysis of the hysteresis curves of the specimens, performance indices of the BRBs were obtained, such as the skeleton curve, the compression bearing capacity increase coefficient, and the energy dissipation index.

1. Skeleton curve

Fig. 12 (p.29) shows the skeleton curves of the specimens, which are almost identical. The core member of each specimen displays an obvious strengthened segment after entering the plastic stage.

2. Compression bearing capacity increase coefficient

The cross-section of the core member tended to increase under compression due to the Poisson effect. Conversely, it tended to decrease under tension, thus leading to an asymmetrical behaviour depending on the loading direction. In addition, the core member may contact the external restraining member when undergoing sufficient lateral distortions and the resultant frictional force at the contact interface will tend to increase the core axial force during the compression phases. Consequently, the multi-wave deformation patterns observed on the core members resulted in an amplification effect. Further, the asymmetry of the tension and compression response of a BRB is also affected by the core axial strain amplitude.

The asymmetry of the tension and compression response of a BRB is usually evaluated by the compression bearing capacity increase coefficient $\beta$, which is defined by

$$\beta_i = \frac{N_{\mathrm{C}i,\max}}{N_{\mathrm{T}i,\max}}, \tag{2}$$

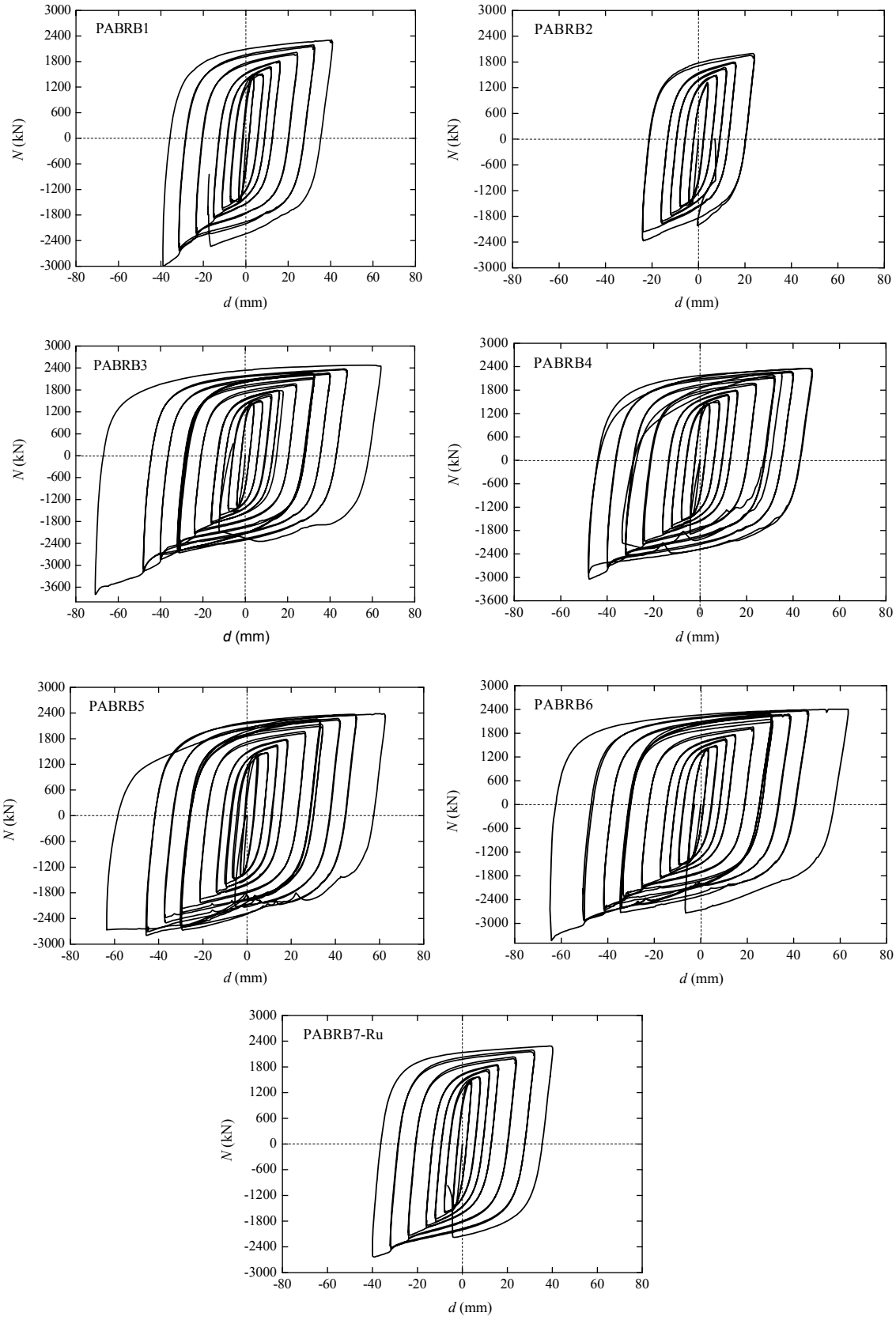


**Fig. 11 Axial load-displacement curves of the specimens**

where $N_{Ti,max}$ and $N_{Ci,max}$ represent the maximum tension and the maximum compression, respectively, during the $i$th hysteresis loop.

ANSI/AISC 341-10 (AISC, 2010) specifies that the compression bearing capacity increase coefficient of a BRB must not exceed 1.3. The coefficients obtained during the distinct loading cycles are shown in Table 4. The increase coefficient of DRT-ABRB remained below 1.3 when the core axial strain remained within 2.00%. Even when the core axial strain reached 2.00%, the DRT-ABRB still exhibited a symmetrical and stable hysteretic behaviour. However, when a larger axial deformation was induced, the coefficient $\beta_i$ became higher than 1.3, mainly because of the multi-wave contact pattern described above.

3. Energy dissipation index

Anti-seismic parameters of the DRT-BRB specimens were obtained from the hysteresis curves and are listed in Table 5. The equivalent damping ratio and the cumulative dissipated energy can reflect

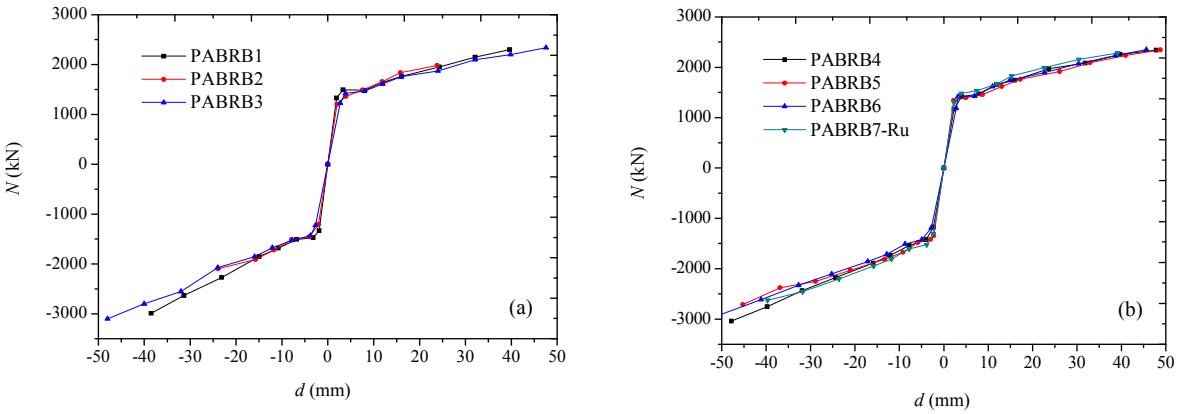


**Fig. 12 Skeleton curves of the specimens**
(a) PABRB1–PABRB3; (b) PABRB4–PABRB7-Ru

**Table 4 Compression bearing capacity increase coefficient of the specimens**

| Specimen | Compression bearing capacity increase coefficient under each core axial strain | | | | | | |
|---|---|---|---|---|---|---|---|
| | 0.25% | 0.50% | 0.75% | 1.00% | 1.50% | 2.00% | 3.00% |
| PABRB1 | 0.987 | 1.014 | 1.026 | 1.049 | 1.163 | 1.225 | – |
| PABRB2 | 1.066 | 1.012 | 1.039 | 1.039 | 1.059 | – | – |
| PABRB3 | 1.009 | 1.040 | 1.039 | 1.054 | 1.107 | 1.217 | 1.325 |
| PABRB4 | 1.001 | 1.047 | 1.046 | 1.086 | 1.104 | 1.169 | 1.299 |
| PABRB5 | 1.013 | 1.013 | 1.034 | 1.030 | 1.061 | 1.078 | 1.155 |
| PABRB6 | 1.005 | 1.057 | 1.060 | 1.065 | 1.109 | 1.123 | 1.241 |
| PABRB7-Ru | 1.027 | 1.045 | 1.082 | 1.067 | 1.107 | 1.138 | – |

**Table 5 Energy dissipation indices of the specimens**

| Specimen | Equivalent damping ratio of the specimens under each core axial strain | | | | | | Cumulative dissipated energy (kN·m) | Cumulative plastic deformation capability |
|---|---|---|---|---|---|---|---|---|
| | 0.25% | 0.50% | 0.75% | 1.00% | 1.50% | 2.00% | | |
| PABRB1 | 0.254 | 0.409 | 0.410 | 0.430 | 0.444 | 0.446 | 1351 | 437 |
| PABRB2 | 0.261 | 0.403 | 0.419 | 0.437 | 0.472 | – | 629 | 229 |
| PABRB3 | 0.288 | 0.403 | 0.423 | 0.440 | 0.466 | 0.457 | 3737 | 1078 |
| PABRB4 | 0.301 | 0.417 | 0.422 | 0.442 | 0.462 | 0.466 | 2784 | 845 |
| PABRB5 | 0.270 | 0.456 | 0.447 | 0.463 | 0.473 | 0.491 | 3451 | 1022 |
| PABRB6 | 0.296 | 0.417 | 0.418 | 0.437 | 0.454 | 0.473 | 3615 | 1042 |
| PABRB7-Ru | 0.254 | 0.409 | 0.417 | 0.446 | 0.472 | 0.481 | 1376 | 439 |

a specimen's capability to absorb seismic energy. The equivalent damping ratio was calculated by

$$\zeta = \frac{S_{\mathrm{AFDEA}}}{2\pi(S_{\Delta\mathrm{OAB}} + S_{\Delta\mathrm{OCD}})}, \tag{3}$$

where $S_{\mathrm{AFDEA}}$ represents the hysteresis loop area of a BRB under one displacement amplitude (Fig. 13). The cumulative dissipated energy corresponds to the area surrounded by the hysteresis curve (Fig. 11), and the cumulative plastic deformation capability can be obtained as

$$\eta = \sum_i \frac{\left| d_{\mathrm{p}i}^{\max} - d_{\mathrm{p}i}^{\min} \right|}{d_{\mathrm{y}}} \tag{4}$$

where $d_{\mathrm{p}i}^{\max}$ and $d_{\mathrm{p}i}^{\min}$ represent the maximum and minimum plastic displacements of the core member, respectively, during the $i$th hysteresis loop, and $d_{\mathrm{y}}$ represents its yield displacement. Eq. (4) can be used to evaluate the deformation capability of a BRB.

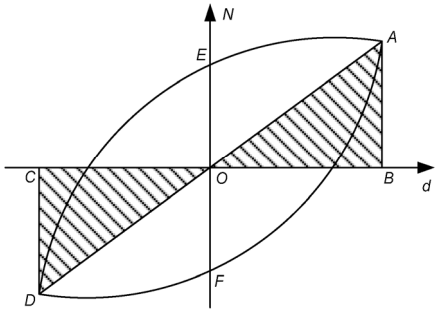


**Fig. 13 Calculation diagram of equivalent damping ratio**

It may be deduced from Table 5 that the specimens' equivalent damping ratio presents a gradual increasing trend with respect to the axial displacement amplitude. Moreover, the equivalent damping ratio appears to become higher than 0.40 once the core axial strain reaches 0.50%. The specimens' cumulative energy dissipation capacity and plastic deformation capability are large. Specimen PABRB2, which had the lowest cumulative plastic deformation capability, still met the requirements of the minimum limit (200) set by the ANSI/AISC 341-10 (AISC, 2010), demonstrating that all the tested specimens exhibited good plastic deformation capability.

## 5 Conclusions

In this study, cyclic loading tests of seven DRT-ABRB specimens were conducted to consider the influence of different design parameters on the hysteretic behaviour and energy dissipation characteristics of DRT-ABRBs and to investigate the failure mechanisms that may arise. Based on the experimental results, the following conclusions can be drawn:

1. When the external cover plate is thinner, the external member end of a DRT-ABRB will easily undergo local pressure-bearing failure. This failure mode can be avoided by implementing reasonable construction measures.

2. When the extended strengthened core region had a smaller stiffness, a larger end rotation of the BRB was observed, which was shown to be disadvantageous to its overall performance.

3. The observed hysteretic behaviour of the DRT-ABRB with restricted end rotation was superior to that of a pure pinned DRT-ABRB. However, the additional bending moment of the BRB's connecting joints tended to increase.

4. All DRT-ABRB specimens showed an excellent energy dissipation performance and verified the rationality of the BRB specimens' construction details, thereby providing a sufficient and reliable basis for engineering applications.

## References

American Institute of Steel Construction (AISC), 2010. Seismic Provisions of Structural Steel Buildings, ANSI/AISC 341-10. AISC, Chicago, USA.

Black, C.J., Makris, N., Aiken, I.D., 2004. Component testing, seismic evaluation and characterization of buckling-restrained braces. *Journal of Structural Engineering*, **130**(6):880-894. http://dx.doi.org/10.1061/(ASCE)0733-9445(2004)130:6(880)

Chen, C.C., Chen, S.Y., Liaw, J.J., 2001. Application of low yield strength steel on controlled plastification ductile concentrically braced frames. *Canadian Journal of Civil Engineering*, **28**(5):823-836. http://dx.doi.org/10.1139/l01-044

Chou, C.C., Chen, S.Y., 2010. Subassemblage tests and finite element analyses of sandwiched buckling-restrained braces. *Engineering Structures*, **32**(8):2108-2121. http://dx.doi.org/10.1016/j.engstruct.2010.03.014

Di Sarno, L., Elnashai, A.S., 2009. Bracing systems for seismic retrofitting of steel frames. *Journal of Constructional Steel Research*, **65**(2):452-465. http://dx.doi.org/10.1016/j.jcsr.2008.02.013

Di Sarno, L., Manfredi, G., 2010. Seismic retrofitting with buckling restrained braces: application to an existing non-ductile RC framed building. *Soil Dynamics & Earthquake Engineering*, **30**(11):1279-1297. http://dx.doi.org/10.1016/j.soildyn.2010.06.001

Di Sarno, L., Manfredi, G., 2012. Experimental tests on full-scale RC unretrofitted frame and retrofitted with buckling-restrained braces. *Earthquake Engineering & Structural Dynamics*, **41**(2):315-333. http://dx.doi.org/10.1002/eqe.1131

Eryaşar, M.E., Topkaya, C., 2009. An experimental study on steel-encased buckling-restrained brace hysteretic dampers. *Earthquake Engineering & Structural Dynamics*, **39**(5):561-581.

Fahnestock, L.A., Ricles, J.M., Sause, R., 2007. Experimental evaluation of a large-scale buckling-restrained braced frame. *Journal of Structural Engineering*, **133**(9):1205-1214. http://dx.doi.org/10.1061/(ASCE)0733-9445(2007)133:9(1205)

Guo, Y.L., Wang, X.A., 2010. A Double Rectangular Tube Assembled Buckling Restrained Brace. China Patent 201020574017.5 (in Chinese).

Guo, Y.L., Jiang, Z.Q., Wang, X.A., *et al*., 2015. Study on restraining stiffness of double rectangular tube assembled buckling-restrained brace. *Engineering Mechanics*, **32**(4):22-32 (in Chinese).

Hoveidae, N., Rafezy, B., 2012. Overall buckling behavior of all-steel buckling restrained braces. *Journal of Constructional Steel Research*, **79**(12):151-158. http://dx.doi.org/10.1016/j.jcsr.2012.07.022

Inoue, K., Sawaizumi, S., Higashibata, Y., 2001. Stiffening requirements for unbonded braces encased in concrete panels. *Journal of Structural Engineering*, **127**(6):712-719. http://dx.doi.org/10.1061/(ASCE)0733-9445(2001)127:6(712)

Iwata, M., Murai, M., 2006. Buckling-restrained brace using steel mortar planks; performance evaluation as a hysteretic damper. *Earthquake Engineering & Structural Dynamics*, **35**(14):1807-1826. http://dx.doi.org/10.1002/eqe.608

Jiang, Z.Q., Guo, Y.L., Wang, X.A., *et al.*, 2015a. Design method of the pinned external integrated buckling-restrained braces with extended core. Part I: theoretical derivation. *Journal of Zhejiang University-SCIENCE A (Applied Physics & Engineering)*, **16**(10):781-792. http://dx.doi.org/10.1631/jzus.A1400325

Jiang, Z.Q., Guo, Y.L., Tong, J.Z., *et al.*, 2015b. Design method of the pinned external integrated buckling-restrained braces with extended core. Part II: finite element numerical verification. *Journal of Zhejiang University-SCIENCE A (Applied Physics & Engineering)*, **16**(10):793-804. http://dx.doi.org/10.1631/jzus.A1400326

Jiang, Z.Q., Guo, Y.L., Wang, X.A., *et al*., 2015c. Theoretical study on design methods for double rectangular tube assembled buckling-restrained braces. *Engineering Mechanics*, **32**(6):41-51 (in Chinese).

Jiang, Z.Q., Dou, C., Guo, Y.L., *et al*., 2017. Theoretical study on design methods for pinned assembled BRB with flat core. *Engineering Structures*, **133**:1-13. http://dx.doi.org/10.1016/j.engstruct.2016.12.004

Ju, Y.K., Kim, M.H., Kim, J., *et al*., 2009. Component tests of buckling-restrained braces with unconstrained length. *Engineering Structures*, **31**(2):507-516. http://dx.doi.org/10.1016/j.engstruct.2008.09.014

Kimura, K., Yoshioka, K., Takeda, T., 1976. Tests on braces encased by mortar in-filled steel tubes. *In:* Summaries of Technical Papers of Annual Meeting, Architectural Institute of Japan, Japan, **1041**:1-42 (in Japanese).

Standardization Administration of the People's Republic of China (SAC), 2010. Metallic Materials–Tensile Testing at Ambient Temperature, GB/T228.1-2010. SAC, Beijing, China (in Chinese).

Sun, F.F., Li, G.Q., Guo, X.K., *et al*., 2011. Development of new-type buckling-restrained braces and their application in aseismic steel frameworks. *Advances in Structural Engineering*, **14**(4):717-730. http://dx.doi.org/10.1260/1369-4332.14.4.717

Tremblay, R., Bolduc, P., Neville, R., *et al*., 2006. Seismic testing and performance of buckling-restrained bracing systems. *Canadian Journal of Civil Engineering*, **33**(2):183-198. http://dx.doi.org/10.1139/l05-103

Tsai, K., Hsiao, P., 2008. Pseudo-dynamic test of a full-scale CFT/BRB frame—Part II: seismic performance of buckling-restrained braces and connections. *Earthquake Engineering & Structural Dynamics*, **37**(7):1099-1115. http://dx.doi.org/10.1002/eqe.803

Usami, T., Wang, C.L., Funayama, J., 2012. Developing high-performance aluminum alloy buckling-restrained braces based on series of low-cycle fatigue tests. *Earthquake Engineering & Structural Dynamics*, **41**(4):643-661. http://dx.doi.org/10.1002/eqe.1149

Wang, C.L., Usami, T., Funayama, J., 2012. Evaluating the influence of stoppers on the low-cycle fatigue properties of high-performance buckling-restrained braces. *Engineering Structures*, **41**(3):167-176.

http://dx.doi.org/10.1016/j.engstruct.2012.03.040

Wang, C.L., Usami, T., Funayama, J., *et al*., 2013. Low-cycle fatigue testing of extruded aluminium alloy buckling-restrained braces. *Engineering Structures*, **46**(1):294-301. http://dx.doi.org/10.1016/j.engstruct.2012.07.016

Xie, Q., 2005. State of the art of buckling-restrained braces in Asia. *Journal of Constructional Steel Research*, **61**(6): 727-748. http://dx.doi.org/10.1016/j.jcsr.2004.11.005

Yoshino, T., Kano, Y., 1971. experimental study on shear wall with braces (Part 2). *In:* Summaries of Technical Papers of Annual Meeting, Architectural Institute of Japan, Japan, **11**:403-404 (in Japanese).

Zhao, J., Wu, B., Ou, J., 2011. A novel type of angle steel buckling-restrained brace: cyclic behavior and failure mechanism. *Earthquake Engineering & Structural Dynamics*, **40**(10):1083-1102. http://dx.doi.org/10.1002/eqe.1071

Zhao, J., Wu, B., Ou, J., 2012. Effect of brace end rotation on the global buckling behavior of pin-connected buckling-restrained braces with end collars. *Engineering Structures*, **40**(7):240-253. http://dx.doi.org/10.1016/j.engstruct.2012.02.030

## 中文概要

**题　目：铰接双矩管装配式防屈曲支撑试验研究**

**目　的：**通过双矩管装配式防屈曲支撑的滞回试验研究，探讨防屈曲支撑可能存在的破坏模式及各设计参数对支撑耗能性能的影响，验证支撑端部构造细节的合理性，提出支撑设计建议。

**创新点：**1. 试验研究铰接双矩管装配式防屈曲支撑的滞回性能；2. 获得 4 种支撑破坏模式。

**方　法：**通过对 7 根铰接双矩管装配式防屈曲支撑的滞回性能试验，研究支撑外围盖板厚度、内核加强翼板高度和外围槽钢翼缘高度等参数对防屈曲支撑破坏机理及耗能性能的影响。

**结　论：**1. 外围盖板厚度太薄，支撑易发生端部折曲破坏；2. 端部转动受限制的支撑，其滞回性能优于纯铰接防屈曲支撑，但支撑连接节点处的附加弯矩不容忽视；3. 支撑均表现出优良的屈曲耗能性能，验证了试验试件端部构造细节的合理性。

**关键词：**双矩管装配式防屈曲支撑；端部构造；滞回性能；破坏模式；高强螺栓